Machine Vision and Applications
DOI 10.1007/s00138-011-0362-8

SPECIAL ISSUE PAPER

Performance of optical flow techniques for motion analysis of fluorescent point signals in confocal microscopy

José Delpiano · Jorge Jara · Jan Scheer · Omar A. Ramírez · Javier Ruiz-del-Solar · Steffen Härtel

Received: 13 October 2010 / Revised: 14 June 2011 / Accepted: 7 July 2011

Abstract Optical flow approaches calculate vector fields which determine the apparent velocities of objects in time-varying image sequences. They have been analyzed extensively in computer science using both natural and synthetic video sequences. In life sciences, there is an increasing need to extract kinetic information from temporal image sequences which reveals the interplay between form and function of microscopic biological structures. In this work, we test different variational optical flow techniques to quantify the displacements of biological objects in 2D fluorescent image sequences. The accuracy of the vector fields is tested for defined displacements of fluorescent point sources in synthetic image series which mimic protein traffic in neuronal dendrites, and for $GABA_BR1$ receptor subunits in dendrites of hippocampal neurons. Our results reveal that optical flow fields predict the movement of fluorescent point sources within an error of 3% for a maximum displacement of 160 nm. Displacement of agglomerated $GABA_BR1$ receptor subunits can be predicted correctly for maximum displacements of 640 nm. Based on these results, we introduce a criteria to derive the optimum parameter combinations for the calculation of the optical flow fields in experimental images. From these results, temporal sampling frequencies for image acquisition can be derived to guarantee correct motion estimation for biological objects.

Keywords Optical flow · Motion estimation · Light microscopy · Fluorescence

Electronic supplementary material The online version of this article (doi:10.1007/s00138-011-0362-8) contains supplementary material, which is available to authorized users.

J. Delpiano · J. Ruiz-del-Solar
Department of Electrical Engineering, Faculty of Physical and Mathematical Sciences, University of Chile, Av. Beauchef 850, Santiago, Chile

J. Delpiano
Faculty of Engineering and Applied Sciences, University of the Andes, Av. San Carlos de Apoquindo 2200, Santiago, Chile

J. Jara · J. Scheer · O. A. Ramírez · S. Härtel (✉)
Laboratory for Scientific Image Analysis (SCIAN-Lab) at the Program of Anatomy and Developmental Biology and the Biomedical Neuroscience Institute BNI, ICBM, Faculty of Medicine, University of Chile, Independencia 1027, Santiago, Chile
e-mail: shartel@med.uchile.cl
URL: http://www.scian.cl

J. Jara
Department of Computer Sciences, Faculty of Physical and Mathematical Sciences, University of Chile, Av. Beauchef 850, Santiago, Chile

1 Introduction

Partnerships between mathematical-computational and experimental disciplines are increasingly important to meet the challenges of modern life sciences. This is especially true for fluorescence-based microscopy which has become a standard tool in bioscience and clinical diagnostics. Today, confocal microscopy techniques are widely available and open the access to *in vivo* observation of three-dimensional biological processes from subcellular to supracellular levels. In parallel to the advances in optics and hardware technologies, improved understanding of the physics of fluorescence phenomena, chemical synthesis of fluorescent molecules, and the advances in molecular genetics have generated new fluorescent probes and proteins which label virtually any cellular component with a specific color. Through a combination of mathematical and computational techniques, processes like diffusion, protein assembly and colocalization [1], vesicle

Published online: 30 July 2011

trafficking, or cellular migration can be studied in cell cultures [2], tissue or entire organisms [3].

The resolution of diffraction limited microscopes is coupled to the full width at half maximum (FWHM) value of the optical point spread function (PSF) and yields ∼250 nm in the xy-plane and ∼750 nm in the z axis. Resolution beyond the diffraction limit can be obtained by novel techniques such as structured illumination microscopy (SIM) [4] or 4π-microscopy [5] which improve resolution by a factor of two. Other approaches such as photo-activated localization microscopy (PALM) localize fluorescent point sources down to the nm-scale [6]. Finally, stimulated emission depletion (STED) [7] leads to theoretically unlimited resolution. In terms of time scales, scanning technologies based on spinning disk microscopy (SDM) or digital scanned laser light sheet fluorescence microscopy (DSLM) [8] allow acquiring 3D images in time scales of milliseconds to seconds. This permits visualizing many relevant dynamic processes *in vivo* for the first time.

For object segmentation and feature extraction, approaches based on partial differential equations (PDEs) [9] yield excellent results for the analysis of morpho-topological descriptors in the field of lipid domain formation [10–13], or developmental biology [3,8]. For motion estimation of biological structures from a subcellular, cellular to a supracellular level, PDE approaches based on optical flow (OF) vector fields have become increasingly important [14–23].

OF was introduced in 1981 by Horn and Schunck (HS) as "… the distribution of apparent velocities of movement of brightness patterns in an image" [24]. The idea contains two basic assumptions: the "gray value constancy" and the "smooth flow of the intensity values" between two successive images. Over the past decades, variations of the original HS-OF approach have been published [25–29]. These so-called combined local global (CLG) methods generalize the "global" HS and the "local" Lucas and Kanade (LK) [30] approaches. The CLG-OF aims to improve the accuracy of the OF field for small-scale variations while retaining the HS-OF benefits of dense and smooth vector fields. The CLG methods still maintain the gray value constancy, while other works report the necessity to loosen this assumption [31,32].

Gray value constancy and smooth flow assumptions make OF especially attractive for the detection of movement of fluorescent signals within image series obtained from optical microscopy. With respect to the gray value constancy, the development of novel fluorescent probes, increasingly stable fluorescent proteins, and improved illumination techniques reduce the impact of photobleaching in many experimental scenarios and the intensity decrease between two consecutive frames becomes negligible [1,2,14,33,34]. With respect to the smooth flow assumption, sophisticated deconvolution algorithms remove Poisson noise to an imperceptible degree prior to OF analysis [12,35–37]. In summary, microscopic image series meet both fundamental assumptions of the OF equations which make this approach extremely promising to meet the requirements for motion estimation in fluorescence microscopy.

In the following, we compare the HS-OF and different CLG-OF approaches for motion estimation of fluorescent point sources in 2D fluorescent images (see Tables 1 and 2). The performance of the OF vector fields is tested with different error measures for defined displacements in synthetic image series which mimic fluorescent protein mobility, and for the displacement of $GABA_B$ receptor subunits in dendrites of hippocampal neurons. In addition, we suggest a criterion to determine the value of the regularization parameter α, in order to minimize the error of the resulting flow field. We determine the limits for the displacement prediction of the OF approaches and relate them to the dimension of the PSF of the microscopic system. Our analysis leads to a suggestion for the optimum temporal acquisition frequency of microscopic images for a given experimental setting.

2 HS- and CLG-approach formulations

The HS-OF approach minimizes a global energy functional over the image data, solving a diffusion-reaction equation that yields dense and homogeneous flow fields. The CLG-OF approach proposed by Bruhn et al. [25,27,28] includes an additional term (J_ρ) that allows locally smoothed flows, based on the Lucas and Kanade formulation [30], in addition to some minor variations that are summarized here. In order to find an optimal solution via PDE systems that are solved iteratively, both methods are defined using a variational formulation.

2.1 HS-OF approach

Horn and Schunck [24] assume "gray value constancy" and "smooth flow" of the intensity values between two images taken at times t_1 and t_2. For an image varying in time $I(x, y, t)$, and particularly for a confocal image, the "gray value constancy", $\mathrm{d}I(x, y, t)/\mathrm{d}t = 0$, can be expressed in form of a first-order Taylor expansion that yields the basic OF constraint equation and leads to the optical displacement vector field $\underline{V} = [u(x, y, t), v(x, y, t), 1]^T$:

$$\begin{aligned} &I(x+u, y+v, t+\Delta t) - I(x, y, t) = 0 \\ &\quad \Rightarrow \quad I_x u + I_y v + I_t = 0 \end{aligned} \tag{1}$$

Integrating over the image domain, Ω, the HS-approach introduces the "smooth flow" constraint weighted by a regularization parameter, α, to define a convex energy functional

Table 1 Discretization of the HS- and CLG-approaches for 2D OF computation

	HS-approach	CLG-approach
Gradient at $I(x_i, y_i, t_k)$	Spatial gradients: $I_x \approx \frac{1}{4}\left(I_{x_{i+1},y_j,t_k} - I_{x_i,y_j,t_k} + I_{x_{i+1},y_{j+1},t_k} - I_{x_i,y_{j+1},t_k} + I_{x_{i+1},y_j,t_{k+1}} - I_{x_i,y_j,t_{k+1}} + I_{x_{i+1},y_{j+1},t_{k+1}} - I_{x_i,y_{j+1},t_{k+1}}\right)$ $I_y \approx \frac{1}{4}\left(I_{x_i,y_{j+1},t_k} - I_{x_i,y_j,t_k} + I_{x_{i+1},y_{j+1},t_k} - I_{x_{i+1},y_j,t_k} + I_{x_i,y_{j+1},t_{k+1}} - I_{x_i,y_j,t_{k+1}} + I_{x_{i+1},y_{j+1},t_{k+1}} - I_{x_{i+1},y_j,t_{k+1}}\right)$	Spatial gradients: $I_x \approx I \otimes \frac{1}{12h}\,[1 \quad -8 \quad 0 \quad 8 \quad -1]_x \,\big\vert_{x_i,y_j,t_{k+1}}$ $I_y \approx I \otimes \frac{1}{12h}\,[1 \quad -8 \quad 0 \quad 8 \quad -1]_y \,\big\vert_{x_i,y_j,t_{k+1}}$ Averaged spatial gradients: $I_x \approx I \otimes \frac{1}{12h}\frac{1}{2}\left([1 \quad -8 \quad 0 \quad 8 \quad -1]_x \,\big\vert_{x_i,y_j,t_k} + [1 \quad -8 \quad 0 \quad 8 \quad -1]_x \,\big\vert_{x_i,y_j,t_{k+1}}\right)$ $I_y \approx I \otimes \frac{1}{12h}\frac{1}{2}\left([1 \quad -8 \quad 0 \quad 8 \quad -1]_y \,\big\vert_{x_i,y_j,t_k} + [1 \quad -8 \quad 0 \quad 8 \quad -1]_y \,\big\vert_{x_i,y_j,t_{k+1}}\right)$
	Time gradient: $I_t \approx \frac{1}{4}\left(I_{x_i,y_j,t_{k+1}} - I_{x_i,y_j,t_k} + I_{x_{i+1},y_j,t_{k+1}} - I_{x_{i+1},y_j,t_k} + I_{x_i,y_{j+1},t_k} - I_{x_i,y_{j+1},t_k} + I_{x_{i+1},y_{j+1},t_{k+1}} - I_{x_{i+1},y_{j+1},t_k}\right)$	Time gradient: $I_t \approx I\left(x_i, y_j, t_{k+1}\right) - I\left(x_i, y_j, t_k\right)$
Laplacian at $I(x_i, y_j, t_k)$	$\Delta u_{x_i,y_j,t_k} \approx U \otimes M \,\big\vert_{x_i,y_j,t_k}$ $\Delta v_{x_i,y_j,t_k} \approx V \otimes M \,\big\vert_{x_i,y_j,t_k}$	
	$M_{h=1} = 3\begin{bmatrix} 1/12 & 1/6 & 1/12 \\ 1/6 & -1 & 1/6 \\ 1/12 & 1/6 & 1/12 \end{bmatrix}_{xy}$	$M_{h=1} = \begin{bmatrix} 0 & 1 & 0 \\ 1 & -4 & 1 \\ 0 & 1 & 0 \end{bmatrix}_{xy}$
Iterative scheme	$u_i^{k+1} = \bar{u}_i^k - \frac{I_x\left(I_x\bar{u}_i^k + I_y\bar{v}_i^k + I_t\right)}{\alpha^2 + I_x^2 + I_y^2}$ $\bar{u}_i^k = \frac{1}{3}\Delta u_i - u_i$	$u_i^{k+1} = \frac{\sum_{l=1}^{2}\frac{\alpha}{h_l^2}\left(\sum_{j\in N_l^-(i)} u_j^{k+1} + \sum_{j\in N_l^+(i)} u_j^k\right) - \left(J_{12i}v_i^k + J_{13i}\right)}{\sum_{l=1}^{2}\frac{\alpha}{h_l^2}\lvert N_l(i)\rvert + J_{11i}}$
	$v_i^{k+1} = \bar{v}_i^k - \frac{I_y\left(I_x\bar{u}_i^k + I_y\bar{v}_i^k + I_t\right)}{\alpha^2 + I_x^2 + I_y^2}$ $\bar{v}_i^k = \frac{1}{3}\Delta v_i - v_i$	$v_i^{k+1} = \frac{\sum_{l=1}^{2}\frac{\alpha}{h_l^2}\left(\sum_{j\in N_l^-(i)} v_j^{k+1} + \sum_{j\in N_l^+(i)} v_j^k\right) - \left(J_{21i}u_i^k + J_{23i}\right)}{\sum_{l=1}^{2}\frac{\alpha}{h_l^2}\lvert N_l(i)\rvert + J_{22i}}$

h step size of the discretized space domain
U, V scalar matrices for u and v components of the OF field
$N_l(i)$ neighbors of pixel i in direction of axis l belonging to Ω
$N_l^+(i) = \{j \in N_l(i) \,|\, j > i\}$, $N_l^-(i) = \{j \in N_l(i) \,|\, j < i\}$
$A\,\big\vert_{x,y,t}$ mask vector/matrix A applied to the image at point (x, y, t). The central element at each mask corresponds to point (x, y, t)
$[a_i]_x$ mask vector is convolved with the image along x axis
$[a_{i,j}]_{xy}$ mask matrix is convolved with the image over xy-plane (image plane)

Table 2 Settings for the OF computation

Setting	Iterative scheme	Laplacian mask	Gradient mask	J_ρ
HS	HS	HS	HS	–
CLG-A	CLG	CLG	HS	$\rho = 0$ (HS-OF functional)
CLG-B	CLG	CLG	CLG	$\rho = 0$ (HS-OF functional)
CLG-C	CLG	CLG	HS	$\rho > 0$ (CLG functional)
CLG-D	CLG	CLG	CLG	$\rho > 0$ (CLG functional)

$$E_{\mathrm{HS}}(\underline{V}) = \int_\Omega \left(\left(I_x u + I_y v + I_t\right)^2 + \alpha\left(|\nabla u|^2 + |\nabla v|^2\right)\right) \mathrm{d}x\mathrm{d}y \quad (2)$$

The regularization parameter $\alpha > 0$ acts as a smoothing factor for the resulting OF.

2.2 CLG-OF approach

The HS functional can also be expressed as

$$E_{\mathrm{HS}}(\underline{V}) = \int_\Omega \left(\underline{V}^T\left(\nabla_3 I \nabla_3 I^T\right)\underline{V} + \alpha\left(|\nabla u|^2 + |\nabla v|^2\right)\right) \mathrm{d}x\mathrm{d}y \quad (3)$$

with

$$\underline{V} = (u, v, 1)^T \quad (4)$$

and

$$\nabla_3 I = (I_x, I_y, I_t)^T \quad (5)$$

Using this notation, the combined local–global (CLG) energy functional (E_{CLG}) introduced by Bruhn et al. [27,29] is defined as

$$E_{\mathrm{CLG}}(\underline{V}) = \int_{\Omega} \left(\underline{V}^T J_\rho(\nabla_3 I)\underline{V} + \alpha \left(|\nabla u|^2 + |\nabla v|^2 \right) \right) \mathrm{d}x\mathrm{d}y \tag{6}$$

with

$$J_\rho(\nabla_3 I) = G_\rho \otimes \left(\nabla_3 I \nabla_3 I^T \right) \tag{7}$$

The convolution $\otimes$ of the derivative term $\nabla_3 I$ with a normalized 2D Gaussian kernel G_ρ (ρ works as a size parameter), results in a spatio-temporal smoothing of the flow field. It is derived from the LK approach [30]: a weighted least squares system that approximates the flow in a small spatial neighborhood ρ. The term of J_ρ can be seen as a local regularization of the flow field. With $\rho = 0$ the Gaussian kernel becomes a matrix with a single element $G_\rho = [1]$; no smoothing occurs, and E_{CLG} becomes equal to E_{HS}.

2.3 Discrete Euler–Lagrange equations

By taking advantage of the notation of Eq. 6 for E_{CLG} definition, which generalizes the definition of the HS-OF approach, a PDE system can be formulated to obtain a solution of a flow field that guarantees the energy minimization of both functionals.

The flow field $\underline{V} = [u(x, y, t), v(x, y, t), 1]^T$ satisfies the Euler–Lagrange equations:

$$\begin{aligned} \alpha\Delta u - (J_{11}u + J_{12}v + J_{13}) = 0 \\ \alpha\Delta v - (J_{21}u + J_{22}v + J_{23}) = 0 \end{aligned} \tag{8}$$

where J_{kl} denotes the elements of the matrix J_ρ. Neumann boundary conditions are assumed:

$$\partial_n u = 0, \quad \partial_n v = 0 \tag{9}$$

At this point, the HS-OF and CLG-OF approaches differ in their discrete formulation and iterative scheme for the Euler–Lagrange equations. This leads to different results for the computed OF field, even when $\rho = 0$ is used in the E_{CLG} formulation (Eq. 6). We summarize the remaining differences in detail in Table 1.

3 Materials and methods

This section describes the preparation and transfection of primary hippocampal neurons, the parameter settings for microscopic data acquisition and deconvolution, and the generation of artificial model dendrites with motile and static point sources.

3.1 Neuronal cultures and transfection

Adult pregnant female Sprague-Dawley E18 rats were purchased from the Catholic University of Chile and killed in CO_2 chambers according to the Guide for Care and Use of Laboratory Animals (1996, USA National Academy of Sciences). Primary hippocampal neurons were prepared, cultured, and transfected with the fluorescent recombinant $GABA_B$ receptor subunit $GABA_BR1$-mRFP as described in [2]. Movement of $GABA_BR1$ receptor subunits was analyzed 24 h post-transfection with SDM.

3.2 Confocal microscopy and deconvolution

Time lapse microscopy was performed with an Olympus BX61WI DSU (Disk Scanning Unit), using a 60x/0.9 LUMPLFL water objective and cellˆR software. Images were recorded with intensity $I(x, y) \in [0, 255]$, and pixel size $\Delta x/\Delta y = 107/107$ nm, slightly above the Nyquist sampling distance. Acquired images were 1376×1038 pixels and were cropped afterwards to 585×180 pixels to focus on a specific region. For $GABA_BR1$-mRFP, excitation and emission wavelength was $\lambda_{\mathrm{exc}} = 543$ nm and $\lambda_{\mathrm{em}} = 560$ nm. We guaranteed that $I(x, y)$ did not saturate and that image background was slightly above zero. Microscopic raw images were deconvolved with Huygens Scripting Software (SVI, Hilversum, Netherlands). The signal-to-noise ratio was adjusted until the deconvolved images were free of pixel noise. Consecutive xy frames were acquired every 30 s over a period of 30 min.

3.3 Model dendrites with defined signal densities, signal trajectories, and optimum microscopic settings

We developed image-processing routines with Interactive Data Language (IDL) (ITT, Boulder, CO). For the generation of synthetic image series with defined degrees of signal densities and trajectories, model dendrites were generated in 128×128 pixel frames at a Nyquist resolution of 40 nm per pixel (uncompressed TIFF files in 8-bit gray scale, see Figs. 1/2). Microscopic PSFs and Nyquist resolution were calculated with commercial Huygens Scripting Software for a 63x/NA = 1.4 oil objective and an excitation/emission wavelength of 488/520 nm. The selected dendrite diameter of 0.84 µm represents a typical value for dendrites of primary hippocampal neurons [1]. As shown in Fig. 1b, three basic elements are needed to construct a model of dendrite point sources: (i) the normalized PSF for the focal xy-plane of the microscopic setup, (ii) the dendrite shaft with a basal initial fluorescence $I_{\mathrm{D}} = 1$, and (iii) randomly seeded point sources with a signal intensity of $I_{\mathrm{S}} = 50$. When the sum of the dendrite image and the signal image are convolved with the microscopic PSF ($(I_{\mathrm{D}} + I_{\mathrm{S}}) \otimes \mathrm{PSF}$), images were found

to be very similar to those of the neuronal system (compare Fig. 1c left and right column) with respect to size, shape, and density of the point signals (Fig. 1c). 10 point signals with $I_S = 50$ were seeded inside the area of the model dendrite ($I_D = 1$) using the Box-Muller transform for uniformly distributed random numbers [38]. For each frame, the sum of dendrite and point signal ($I_D + I_S$) was convolved with the microscopic PSF. Two of the point sources were set to perform uniform movement of one pixel per frame along the dendrite axis (see arrows in Fig. 1c right column). In addition, we generated single, moving point sources without the underlying dendrite in order to evaluate and compare the different OF approaches (Table 2) with the simplest possible model (Figs. 3, 4 and Online Resource 1–3). The analysis of vertically moving point sources along the model dendrite was identical to the analysis of isolated point sources regarding the maximum prediction of the confined displacement (compare Fig. 3d and Online Resource 1e).

3.4 Error measures for OF fields for motion estimation

We used three different error measures to evaluate the accuracy of the OF field for motion estimation: the average endpoint error (AEE), the average angular error (AAE), and a simplified error for motion only in the vertical axis, the absolute difference error, in the following named "prediction error".

Prediction error will consider a region of interest (ROI) resulting from segmentation of point signals. The prediction error is defined as the absolute difference between the ground truth (defined vertical displacement) v_{gt} and the average value of the estimated vertical component $\bar{v}_{est}$ inside a ROI:

$$\text{prediction error (ROI)} = \left| v_{gt} - \bar{v}_{est}(\text{ROI}) \right| \tag{10}$$

AEE measures the average magnitude of the vector difference between ground truth and estimated flow vectors, while the AAE measures the error as average angular deviation between velocities represented as 3D space–time vectors as defined previously [39].

3.5 Image and data processing

HS-OF was implemented in IDL while the CLG-OF approaches were implemented in C/C++ as dynamic link libraries using Visual Studio 2005 (Microsoft Corp., Redmond, WA). We used SCIAN-Soft implemented in IDL for image handling, segmentation of fluorescent point sources in ROIs, visualization of OF fields, and data analysis. The results were generated on a PC with Windows 7 64-bit and the calculations were represented internally with double precision numbers. Data plots were generated with OriginPro 8.0 (OriginLab Corp., Northampton, MA).

4 Results and discussion

In this section, we describe the experiments performed with synthetic and experimental microscopic images in order to test the accuracy of the computed OF using the HS- and the CLG-approaches summarized in Table 2. In addition, we discuss the suitability of these approaches to capture the movement of fluorescent proteins in a biological dataset acquired with confocal microscopy. Figures 2, 3 and 4 show the results of OF computations with synthetic models performed to analyze the differences between the HS- and CLG-approaches. Figure 5 shows the application of CLG-approaches for the motion estimation of $GABA_BR1$ receptor subunits inside a neuronal dendrite.

4.1 Fluorescent point sources in neuronal and model dendrites

Figure 1 shows examples for the motion of point sources in neuronal and model dendrites. A representative confocal image of a temporal sequence for $GABA_BR1$ receptors in a neuronal dendrite is shown in Fig. 1a. For the calibration of the applied OF techniques, we simulated motion of two point sources inside the model dendrite that mimics the kinetics of fluorescent $GABA_BR1$ signals in the primary hippocampal neurons (see arrows in Fig. 1c), or we used a single moving point source with a background of zero (Figs. 3, 4).

Similarly generated synthetic model images have been used previously for the calibration of algorithms to quantify colocalization of point sources in different fluorescent channels [1,40,41]. The calculated microscopic PSF and the Nyquist distance guarantee the optimum parameters for the acquisition of diffraction limited microscopy images. We restricted our experiments to these optimum settings since the effects of different scale levels and resolution on OF fields have been discussed in detail before [21,42]. For microscopic images, different scales (generated by different PSFs) change the size of point sources in an image which improves the motion estimation of OF-fields for increasing diameters [21]. Variation of the Nyquist sampling frequency induce over- or undersampling of the point sources and was therefore neglected in this study.

In addition, we did not consider the effect of Poisson noise in our study for two reasons: (i) we consider that the removal or smoothing of Poisson noise is part of the image restoring through PSF deconvolution prior to motion estimation by OF. During deconvolution, the signal-to-noise ratio can be set in order to generate images which are almost free of pixel noise. To this end, sophisticated deconvolution software based on solid physical and probabilistic criteria should be preferred [1,43,44]. (ii) Gerencser and Nicholls [21] presented images with different signal-to-noise ratios and discussed the impact on OF fields. In their study, wider spatial differentiation

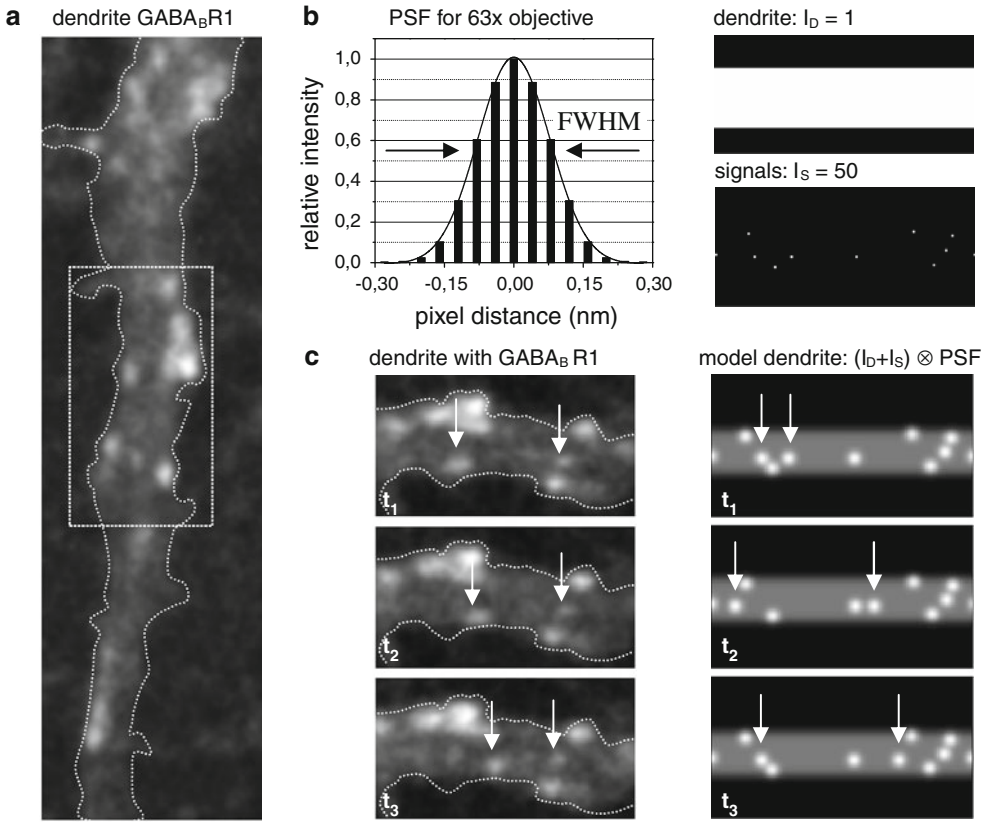

Fig. 1 Motion of point sources in neuronal and model dendrites. **a** Representative image of a dendrite of a primary hippocampal neuron from an experimental movie acquired with spinning disk microscopy (30 min, one frame per 30 s, pixel size is 107 nm in x and y, image size is 585 × 180 pixels). Fluorescence intensity corresponds to the fluorescent $GABA_B$ receptor subunit $GABA_BR1$-mRFP. The rectangle indicates the image section presented in (**c**). **b** Generation of a model dendrite. *Left* channel specific point spread function (PSF), calculated for the acquisition parameters of the microscopic setting used in (**a**). *Right* binary image of a model dendrite with intensity $I_D = 1$ (*right top*) and 10 point signals with intensity $I_S = 50$ (*right bottom*). **c** Motion of $GABA_BR1$ subunits in neuronal dendrite (*left column*) and motion of point sources in model dendrites (*right column*). The model dendrite was generated by the convolution of the sum of the dendrite image and the point signals ($I_D + I_S$) with the PSF (see **b**). For the neuronal dendrite, two moving point sources are pointed out by *arrows* for three consecutive time intervals (t_1–t_3). For the model dendrite, t_1–t_3 represent randomly selected shots of the time sequence

kernels (Savitzky-Golay kernels) improve noise tolerance due to additional smoothing effects. For our study, an additional smoothing parameter within the OF scheme would distract from the principal goal of comparing the HS and the CLG approaches and was therefore neglected.

4.2 HS-OF approach for the prediction of displacements of synthetic and fluorescent point sources

Figure 2 shows HS-OF fields for moving fluorescent point sources in neuronal dendrites (Fig. 2a–c) and model dendrites (Fig. 2d–f). In order to evaluate if a flow field can estimate the movement of the point sources reliably, we segmented fluorescent point signals in ROIs with previously described procedures [1]: in short, we applied Laplace filters in combination with threshold settings in the intensity intervals of the filtered images. Our approach yields much better results than direct setting of thresholds in the intensity image and has been applied successfully for the segmentation of different fluorescent structures in microscopic images in the past [2,35–37]. Figure 2c, f shows representative HS-OF fields calculated with 200 iterations and regularization parameter $\alpha = 10$. 200 iterations were used for all performed experiments, since the relative change of the OF field decreases below 0.4% (see Online Resource 1d). In both cases, smooth and regular vector field patterns are generated. In order to obtain a single value for the prediction of the displacement of the point sources by the OF vector fields, we calculated the average vertical values of the OF fields inside the ROIs $\bar{v}_{est}$ (see Sect. 3.4).

HS-OF vector fields are sensitive to the value of the global regularization parameter α. Figure 3 shows the effect of α for the prediction of point source displacements. HS-OF fields were calculated for defined displacements of the point source

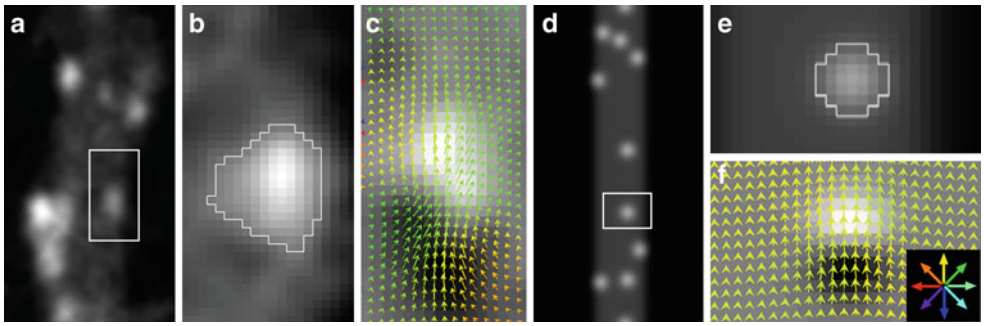

Fig. 2 HS-OF approach for detection of moving point sources in neuronal dendrites and model dendrites. **a** Fluorescence image $I(x, y, t_i)$ of a neuronal dendrite with moving point source (*square*). **b** Zoom of a moving point source (square in **a**). The *white line* marks the ROI of the fluorescent point source after segmentation. **c** HS-OF field calculated for image in (**b**) at time t_i ($I(x, y, t_i)$) and time t_{i+1} ($I(x, y, t_{i+1})$). The background image shows the time derivative of the image intensities $I(x, y, t_{i+1}) - I(x, y, t_i)$. The minimum and maximum values of the time derivative were scaled to $I \in [0, 255]$. Orientation of the vector field is color coded (see **f**, bottom right). HS-OF field was calculated with 200 iterations, regularization parameter α was set to 10. **d** Model dendrite $I(x, y, t_i)$ with moving point sources. **e** Zoom of a moving point source (square in **d**). The *white line* marks the ROI of the point source after segmentation. **f** HS-OF field calculated for image in **e** ($I(x, y, t_i)$) after the translation of the point source one pixel towards the top ($I(x, y, t_{i+1})$). Direction is color coded (*bottom right*). The background image and the HS-OF field were calculated as described in (**c**)

between 1 and 8 pixels (Fig. 3d). Each data point represents the average vertical value of the HS-OF ($\bar{v}_{\text{est}}$), calculated inside the segmented ROIs (see Fig. 2e). As can be observed, high α-values ($\alpha = 200$) attenuate the OF field severely: the predicted point source displacement is underestimated for all displacements (see Fig. 3c, d). With decreasing α, the prediction of the displacement improves, until it reaches an optimum for $\alpha = 90$ (see Fig. 3b, d). The optimum α can be chosen from the prediction error-plot which shows a common minimum at $\alpha = 90$ for displacements of 1–4 pixels (Fig. 3e). With $\alpha = 90$, displacements from 1–4 pixels are predicted almost perfectly by the flow field (see Fig. 3d, e). With $\alpha < 90$, the prediction for the displacements of 1–2 pixels shows almost the same precision as with $\alpha = 90$, but increasingly overestimates displacements from 3–4 pixels. Correct predictions of displacements above 4 pixels can only be obtained by chance due to the crossing of the prediction curves for $\alpha < 90$ with the control (Fig. 3d, black circles); this effect is due to the corresponding OF fields, which produce vectors with crossing directions (see Fig 3a right).

For displacements of 1–4 pixels, the maximum prediction error yields 0.11 pixels. Such errors can be regarded small for practical purposes: considering the resolution of diffraction limited microscopy and the corresponding Nyquist sampling distance of 40 nm per pixel (correct sampling distance for experiments on a sub cellular or cellular level [45]), the prediction error is less than 4.4 nm. Since the diffraction limited resolution of optical microscopy is coupled to the FWHM-value of the corresponding PSF (200 nm for the selected settings, see Fig. 1b), the HS-OF approach predicts point source displacements up to 160 nm with an error below 3%. For point source displacements above 160 nm, the HS-OF fields start to produce vector crossings and points of convergence or divergence (Fig. 3a, b, $d \geq 5$).

We have also checked the performance of HS-OF fields for 12-bit images after rescaling 8-bit to 12-bit images. The results obtained for 12-bit images show no substantial difference to the 8-bit plots; the sensitivity to the global regularization parameter α shifts to higher orders (compare Online Resource 1c and Fig. 3d).

4.3 CLG-OF approaches for the prediction of displacements of microscopic point sources

We analyzed different CLG-OF approaches (CLG-A-D), under the variation of the global regularization parameter α, the local derivative smoothing parameter ρ, and different gradient masks (see Table 2):

- **CLG-A**: OF fields were calculated without derivative smoothing J_ρ ($\rho = 0$) and with the gradient mask of the HS-OF approach, as a function of point source displacement d and the regularization parameter α. The results show very similar characteristics to the HS-OF approach presented in Fig. 3d, e (see Online Resource 2a, b). The remaining differences can be explained by the Laplacian discretization and the iterative scheme used for the CLG-OF approach (see Table 1). The computed CLG-OF fields are optimized with a slightly higher regularization parameter $\alpha = 110$. Again, the prediction of the point source displacement is reliable for distances of up to 4 pixels, and the minimum prediction error value is very close to the HS-OF approach (compare Fig. 3e and Online Resource 2b). In summary, both approaches lead to virtually the same results.

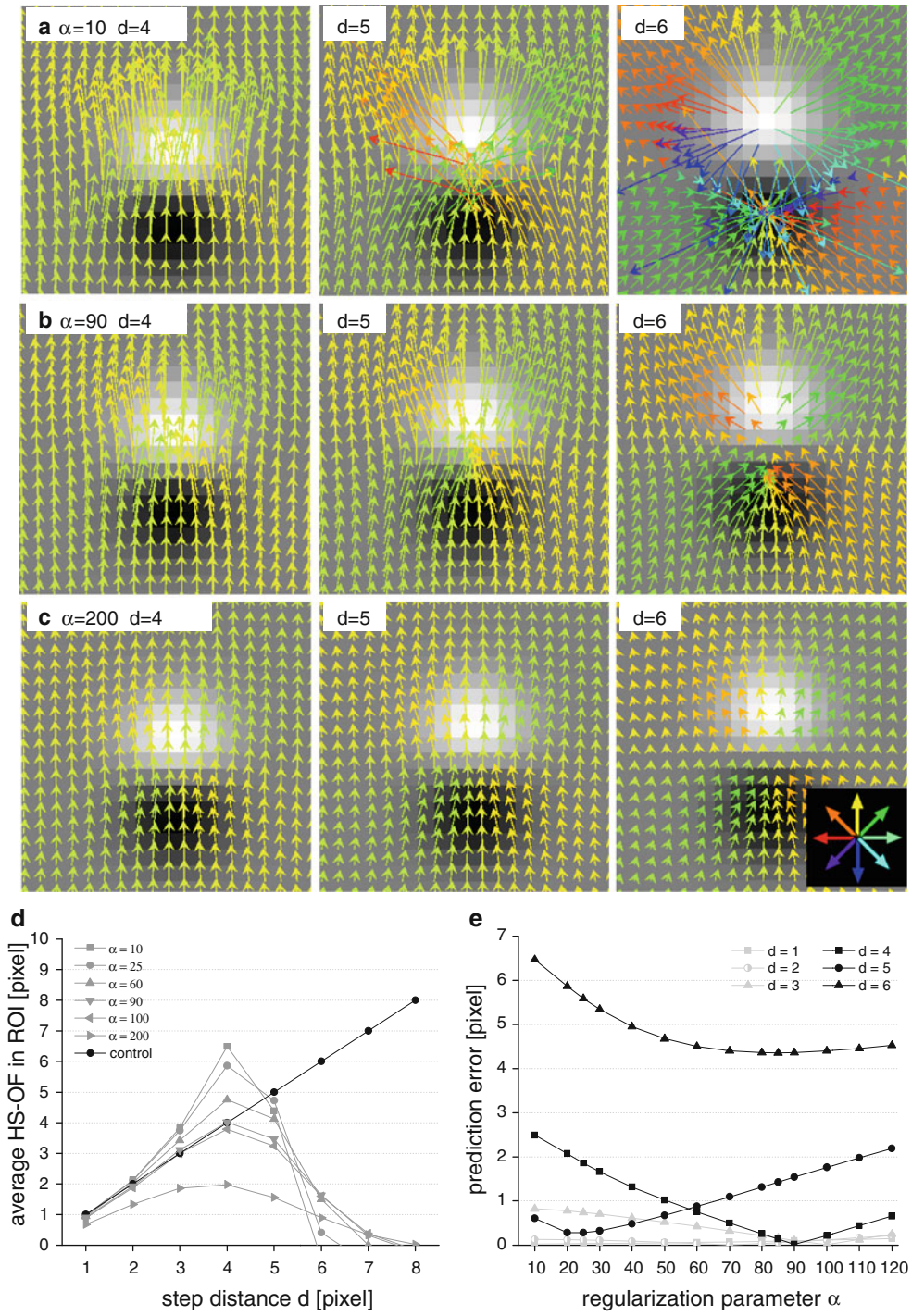

Fig. 3 Flow fields and prediction of point source displacement by HS-OF varying the global regularization parameter α. **a**–**c** HS-OF vector fields for different defined vertical displacements $d = 4$–6 pixels and different global regularization parameter values $\alpha = 10$ (**a**), $\alpha = 90$ (**b**), and $\alpha = 200$ (**c**). The background image was calculated as described in Fig. 2c. Direction of the vector fields are color coded (**c**, bottom right). **d** Prediction of point source displacement by the HS-OF approach. Point source displacements were calculated as the average of the vertical component of the HS-OF field inside the ROI (Fig. 2e) depending on the step distance d and varying the global regularization parameter $\alpha = 10, 25, 60, 90, 100, 200$ (*gray lines* and *symbols*). The ground truth displacement of the model point source was plotted for displacements $d = 1$–8 pixels (*black lines* and *symbols*). **e** Prediction error of point source displacement by HS-OF in dependence on the global regularization parameter α. The absolute values of the prediction errors between the HS-OF fields and the displacement of the point source were plotted as a function of the global regularization parameter α and different ground truth displacements $d = 1$–6 pixels (see *symbols*)

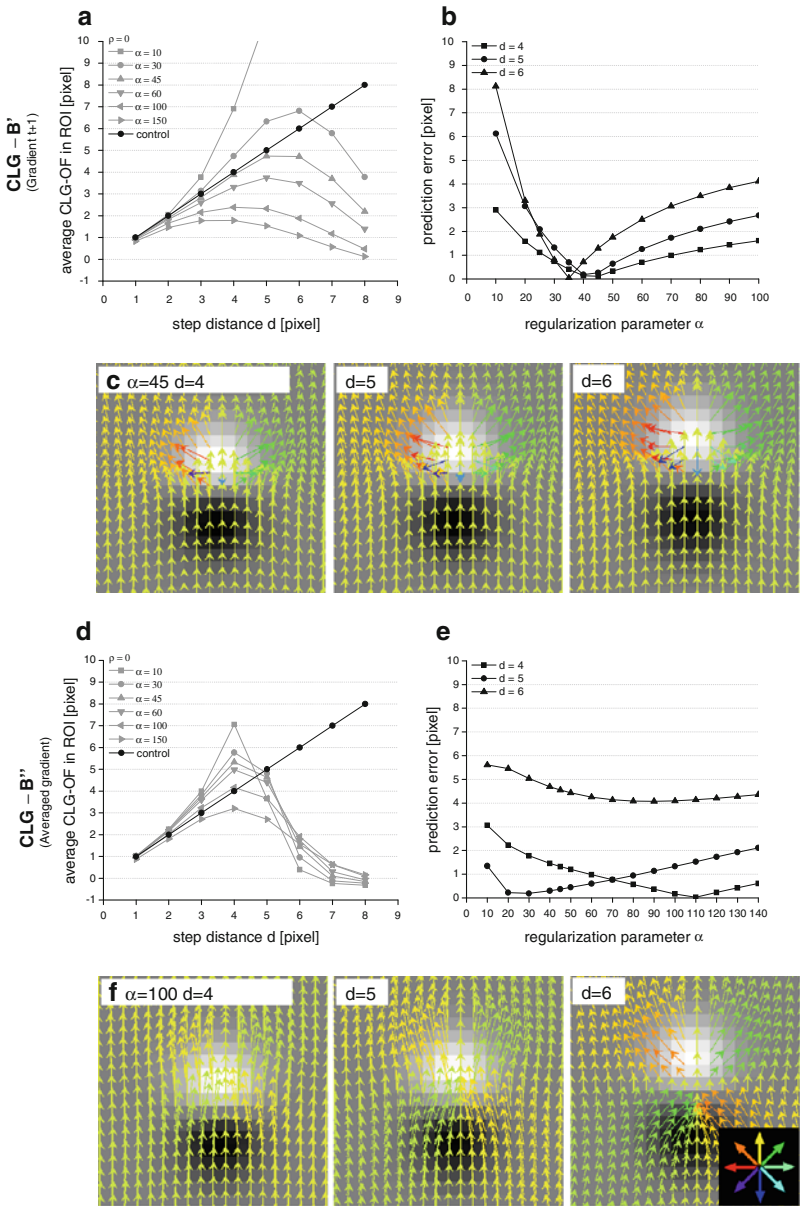

Fig. 4 Prediction of point source displacements and flow fields by CLG-OF varying the global regularization parameter α, gradient masks by Bruhn, and without local derivative smoothing. **a** Prediction of point source displacement as calculated by the CLG-OF approach by Bruhn depending on the step distance d and varying the global regularization parameter $\alpha = 10, 30, 45, 60, 100, 150$. The CLG-OF field was calculated without local derivative smoothing $J_\rho(\rho = 0)$ and the gradient mask used by Bruhn *applied only in the second image frame* (see Table 1). The ground truth displacement of the model point source was plotted for displacements $d = 1$–8 pixels (*black lines* and *symbols*). **b** Prediction error of point source displacement by CLG-OF presented in **a** with respect to the global regularization parameter α. The absolute values of the errors for the prediction between the CLG-OF fields and the displacement of the point source were plotted as a function of the global regularization parameter α and different ground truth displacements $d = 4, 5$, and 6. **c** CLG-OF vector fields for different displacements $d = 4$–6 pixels were calculated without $J_\rho(\rho = 0), \alpha = 45$ and with the gradient mask used by Bruhn *applied only in the second image frame* (see Table 1). The background image was calculated as described in Fig. 2c. Direction of the vector fields are color coded (**f** bottom right). **d** Prediction of point source displacement as calculated by the CLG-OF approach by Bruhn depending on the step distance d and varying the global regularization parameter $\alpha = 10, 30, 45, 60, 100, 150$. The CLG-OF field was calculated without local derivative smoothing J_ρ $(\rho = 0)$ and the *averaged gradient mask of two consecutive frames* used by Bruhn (see Table 1). The ground truth displacement of the model point source was plotted for displacements $d = 1$–8 pixels (*black lines* and *symbols*). **e** Prediction error of point source displacement by CLG-OF presented in **d** with respect to the global regularization parameter α. The absolute values of the errors for the prediction between the CLG-OF fields and the displacement of the point source were plotted as a function of the global regularization parameter α and different ground truth displacements $d = 4, 5$, and 6. **f** CLG-OF vector fields for different displacements $d = 4$–6 pixels were calculated with J_ρ $(\rho = 0), \alpha = 100$, and with the *averaged gradient mask of two consecutive frames* used by Bruhn (see Table 1). The background image was calculated as described in Fig. 2c. Direction of the vector fields are color coded (**f** bottom right)

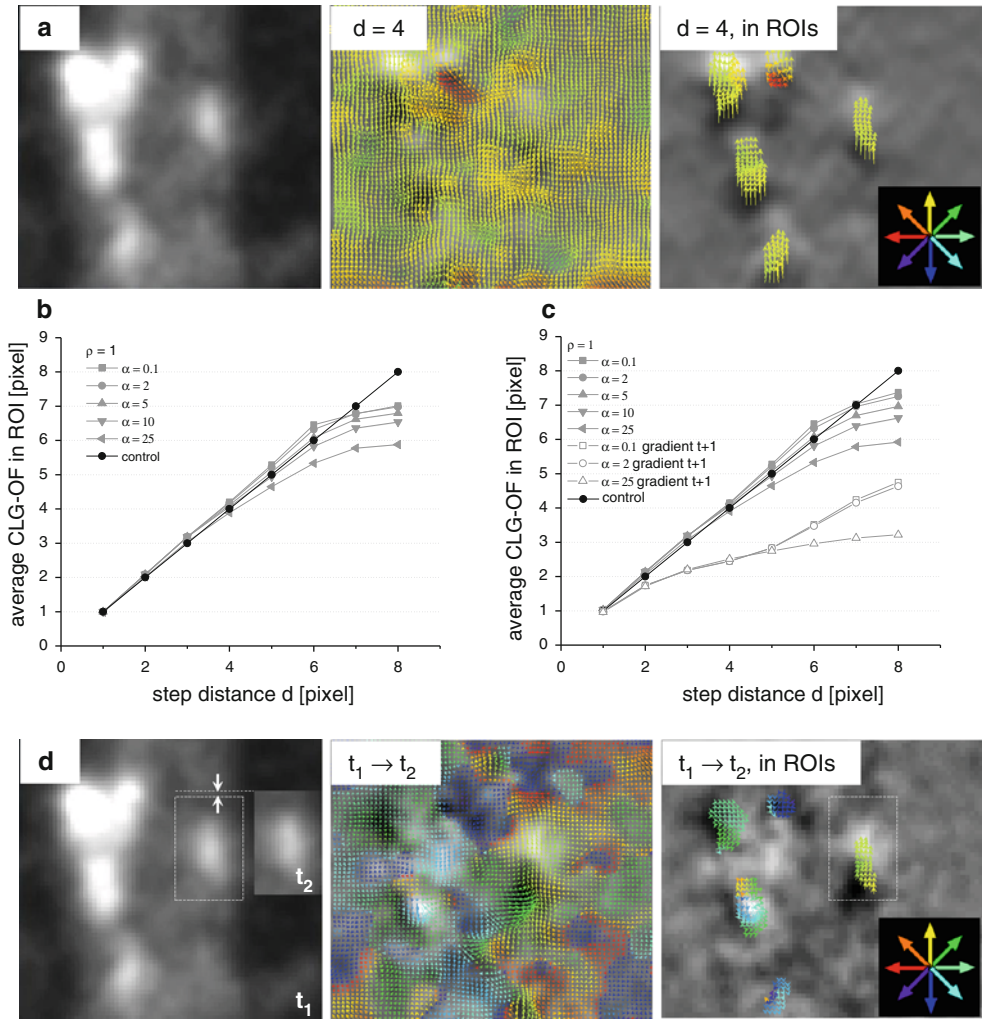

Fig. 5 Prediction of point source displacements by CLG-OF in neuronal dendrites. **a** *Left* Section of the neuronal dendrite shown in Fig. 2. *Center* CLG-OF field calculated between the original image and the same image with a displacement $d = 4$ pixels towards the top with $\alpha = 5$, $\rho = 1$, and the gradient mask of the HS-approach (see Table 1). The background image was calculated as described in Fig. 2c. *Right* CLG-OF shown in segmented ROIs. Direction of the vector fields are color coded (*bottom right*). **b** Point source displacement as calculated by the average of the vertical component of the CLG-OF field inside the ROIs depending on the step distance d and varying the global regularization parameter $\alpha = 0.1, 2, 5, 10, 25$ (*gray lines* and *symbols*). The CLG-OF-field was calculated with local derivative smoothing $J_\rho(\rho = 1)$ and the *gradient mask of the HS-approach* (see Table 1). The ground truth displacement was plotted for displacements $d = 1$–8 pixels towards the top (*black lines* and *symbols*). **c** Point source displacement as calculated by the average of the vertical component of the CLG-OF field inside the ROIs depending on the step distance d and varying the global regularization parameter $\alpha = 0.1, 2, 5, 10, 25$. The CLG-OF-field was calculated with local derivative smoothing $J_\rho(\rho = 1)$, the *averaged gradient mask between two consecutive frames* used by Bruhn (see Table 1), and using the *gradient mask calculated only in one of the image frames*. The ground truth displacement was plotted for displacements $d = 1$–8 pixels towards the top (*black lines* and *symbols*). **d** *Left* Neuronal dendrite region shown in **a** for t_1. *Inset* shows the displacement of the $GABA_B$ receptor subunit $GABA_BR1$-mRFP at t_2. *Center* CLG-OF vector field calculated between images at t_1 and t_2 with $\alpha = 5$, $\rho = 1$, and the gradient mask of the HS-approach (see Table 1). The background image was calculated as described in Fig. 2c. *Right* CLG-OF shown at ROIs. *Arrow* direction is color coded (*bottom right*)

- **CLG-B**: OF fields were calculated without derivative smoothing J_ρ ($\rho = 0$), and two different ways of calculating the image gradients. As introduced by Bruhn et al. [25,28,46], the gradients I_x and I_y were calculated as shown in Table 1: the second-order Taylor approximations of the derivatives were calculated only in one image. Our results show OF fields with gradients calculated at time t_{i+1}. As can be observed in Fig. 4a, b, this approach leads to results that are very different from the HS-OF approximation. The predicted displacements are more sensitive to α, but for an optimum $\alpha = 45$, the prediction improves for displacements of up to 5 pixels. The OF fields show a fundamental difference: they are insensitive to the convergence induced by the

"intensity sink" (dark spot in Fig. 4c), but maintain sensitivity to the divergence induced by the "intensity source" (bright spot in Fig. 4c). This can be explained by the calculation of the gradient at time t_{i+1} that does not take into account time t_i. If the gradient is calculated at time t_i, the OF fields are sensitive to the convergence, and insensitive to the divergence (not shown).

In order to circumvent this problem, we calculated I_x and I_y as the average of the gradients calculated at time t_i and t_{i+1}. The results shown in Fig. 4d–f are very similar to the HS-OF approximation (3d/e) and do not reveal any significant improvement. Similar to the CLG-A approach, the computed CLG-B-OF fields are optimized for a slightly higher α-value ($\alpha = 110$) and allow the prediction of the point source displacements up to 4 pixels. However, the computed CLG-B-OF fields show an improved vertical alignment compared with the results of HS-OF, which is reflected by a lower AAE (see Online Resource 2h).

- **CLG-C**: OF fields were calculated with derivative smoothing J_ρ ($\rho = 1$), and with gradient mask of the HS-OF approach. As Online Resource 2c/d shows, the setting leads to results that are similar to the HS-OF and CLG-A approaches (Fig. 3d, e and Online Resource 2a/b). CLG-C does not improve the prediction errors nor does it allow to predict step distances greater than 4 pixels. The vector fields show a slightly improved alignment in the direction of the vertical displacement (not shown) which results in a slightly lower AAE (see Online Resource 2h).
- **CLG-D**: OF fields were calculated with derivative smoothing J_ρ ($\rho = 1$), and the two different ways of calculating the image gradients (see CLG-B). For both gradients, the results were similar to those obtained by CLG-B (see Fig. 4a–f). Using the averaged gradient mask, the optimum regularization parameter $\alpha = 120$ permits the prediction of the point source displacement up to 4 pixels (Online Resource 2e/f). For this case, we also show the dependence of the OF fields for different ρ-values (Online Resource 3): increasing ρ does not permit to predict step distances greater than 4 pixels, but results in a decreased sensitivity to α. In addition, increasing ρ leads to a lower AAE (Online Resource 2h), probably due to the effect of enhanced local smoothing by J_ρ.

In summary, the HS approach and all tested CLG-approaches show very similar behaviours (except those based on single image gradient masks). None of the methods allows the prediction of step distances greater than 4 pixels (160 nm). However, they are all able to make very precise step predictions for distances less than or equal to 4 pixels. Despite observed differences with respect to the sensitivity to α and the variations of the AAE, the AEE-plot shows that all data points are distributed within a narrow band (AEE <0.25, Online Resource 2g).

4.4 OF approaches for the prediction of $GABA_BR1$-mRFP mobility in neural dendrites

The determination of dynamic parameters of organelle mobility (trajectory length, continuity, direction, and velocity) from image series has been elusive in most biological cases. Previous works have performed particle tracking by either manual or semiautomatic methods [47–49], or by using kymographs [50]. Both techniques work well in systems where the moving structures are clearly distinguishable, for example, mitochondria transport in axons; however, they fail to give accurate measurements on more complex scenarios. This had precluded the study of the dynamics of most organelles in densely populated regions like the soma or the mobility of cargo inside of highly interconnected structures such as the endoplasmic reticulum, which synthesizes and transports secreted and membrane proteins. The application of optical flow techniques to address organelle mobility has been tested in at least two studies, the first concerning the traffic of the endoplasmic reticulum-Golgi intermediate compartment (ERGIC) [19], and the second addressing the transport of mitochondria in hippocampal neurons [21]; the latter specifies the parameters for image acquisition in order to optimize optical flow calculations. Here we show an application of the optical flow for the transport of $GABA_B$ receptors, whose $GABA_BR1$ subunit is retained and transported inside the endoplasmic reticulum of hippocampal neurons [2]. The densely packed particles resulting from the transfected fusion protein $GABA_BR1$-mRFP in dendrites of hippocampal neurons make this system difficult to track, but still suitable for optical flow analysis under optimal image acquisition parameters. Thus, fundamental questions relating dynamical transport of neurotransmitter receptors in dendrites with their function modulating synaptic transmission can be addressed quantitatively, giving insights into their tight underlying temporal and spatial regulation.

We tested CLG-C and CLG-D approaches to predict $GABA_BR1$-mRFP mobility in hippocampal dendrites from DSU image sequences. Considering the results in the previous section, CLG-C was used in representation of all other approaches, as well as CLG-D, in order to test the apparent advantage of the gradient calculated at time t_{i+1} for the prediction of point source movements. For biological image sequences, ground truth data for moving point sources cannot be generated per se, which impedes the identification of optimum values for the global regularization parameter α. Some of the $GABA_BR1$-mRFP subunits are immobile, while others move along the dendrite shaft with unknown displacements.

In order to find the optimum α-values in such sequences, we mimic ground truth data by the following strategy: first

we segment ROIs of fluorescent point sources as described previously [1,2] in a representative image (Fig. 5a); then we apply defined pixel displacements d of the entire image frame to generate the time component t_{i+1} and calculate the OF fields; finally, we plot the predicted value (average) inside these ROIs in dependence of the displacements d and the prediction error as a function of α (Fig. 5a–c).

An example of the flow fields calculated inside the ROIs for a vertical displacement of $d = 4$ pixels can be observed in Fig. 5a (right). From Fig. 5b, it becomes clear that $\alpha = 5$ minimizes the prediction errors for all distances. For our example, the approach includes $GABA_BR1$-mRFP displacements of up to 6 pixels. Taking into account the pixel size of the DSU setting (107 nm per pixel), the maximum displacement of the $GABA_BR1$-mRFP subunits which can be predicted correctly is approximately 650 nm. In comparison with the model dendrite, the experimental image series is undersampled by a factor of 2, due to the optical setup of our DSU. In addition, $GABA_BR1$-mRFP trafficking apparently does not occur on a single subunit basis, since the observed fluorescence signals provide FWHM-values beyond the limits of the theoretical PSF (Fig. 1b). Under these conditions, the maximum distance for precise motion prediction increases from 160 nm in model dendrites to 650 nm under the specific experimental settings. These results are in agreement with the findings published by Gerencser and Nicholls [21] where the maximum distance for precise motion prediction increases with the size of the point sources. In addition, displacements of up to 11 pixels were predicted in fluorescent image sequences of subcellular chromatin structures (nucleoli) with AAE $< 4°$ using a CLG-OF approach with $\alpha = 6$ [14]. Unfortunately, the authors do not comment on pixel size. This rather large estimation can be explained by the broad intensity distribution of the nucleoli. Our experiments for the point source show equally low AAE $< 4°$ using CLG-OF.

The same regularization parameter $\alpha = 5$ optimizes the CLG-D approach for the averaged gradient mask and correctly predicts the displacement up to 6 pixels (Fig. 5c, closed gray symbols). In contrast, the CLG-D approach for the single gradient mask at t_{i+1} (Fig. 5c, open gray symbols), fails for displacements $d \geq 2$ pixels. The apparent advantage of the single gradient mask approach which we observed for the synthetic point sources in Fig. 4a–c could not be validated in real microscopic sequences. These findings suggest that time averaging of the spatial image gradients is necessary in order to obtain reliable predictions within the limits.

For practical purposes of many cell biological experiments which might or might not meet the Nyquist distance, our approach to mimic ground truth by defined displacements in combination with the segmentation of selected ROIs can determine optimum α-values and the maximum range for reliable motion estimation by the OF fields. From the maximum range for reliable motion estimation and the expected object velocities, the optimum time sampling rate can be determined to ensure that the object displacements are captured accurately by the OF fields.

We used the optimum α-value to predict $GABA_BR1$-mRFP trafficking in our microscopic sample sequence. The example in Fig. 5d shows the calculated CLG-OF field for two consecutive image frames (Fig. 5d, center) and the prediction of the $GABA_BR1$-mRFP displacement towards the top of the image (compare Fig. 5d, left and right image). The obtained results fit the observation in the natural image sequence within the limits of the pixel resolution.

5 Conclusions

The comparison of the HS-OF and different CLG-OF approaches for the accurate prediction of displacements of point sources in model dendrites did not reveal substantial differences among the methods: point source displacements were predicted up to a maximum of 4 pixels (160 nm) with very low prediction errors below 3%. In an experimental image series, displacements of moving $GABA_BR1$ receptor subunits in neuronal dendrites could be predicted correctly up to 6 pixels (642 nm). From these values, the temporal sampling frequencies can be calculated for a given experiment in order to guarantee correct motion estimation of fluorescent objects.

One advantage of the CLG-OF approach consists in a reduced sensibility towards the global regularization parameter α. In order to ease the access to the correct parameter settings for the α-values and the parameter ρ for local derivative smoothing, we are currently implementing an automated algorithm to mimic ground truth for defined displacements of signals in biologic image data. Finally, we are expanding the HS- and CLG-OF approaches on a 3D level in order to access vesicle, nucleus, and membrane displacements for applications in different biologic disciplines. Promising results in this field based on OF approaches have been published recently [20].

Acknowledgments The authors would like to give special thanks María Osorio-Reich for her insightful comments on the paper. J. Delpiano and J. Jara are funded by a PhD scholarship from CONICYT (Chile). O. A. Ramírez is funded by FONDECYT (3110157). Research in SCIAN-Lab (S. Härtel) is funded by FONDECYT (1090246) and FONDEF (D07I1019). SCIAN-Lab is member of the German-Chilean Center of Excellence Initiative for Medical Informatics (DAAD), BNI (ICM P09-015-F), and the Advanced Imaging & Bioinformatics Initiative AI·BI (http://www.aibi.cl).

References

1. Ramírez, O.A., García, A., Rojas, R., Couve, A., Härtel, S.: Confined displacement algorithm for the discrimination of true and random colocalization of fluorescence signals in confined cellular compartments. J. Microsc. **239**(3), 173–183 (2010)

2. Ramírez, O.A., Vidal, R.L., Tello, J.A., Vargas, K.J., Kindler, S., Hartel, S., Couve, A.: Dendritic assembly of heteromeric gamma-aminobutyric acid type B receptor subunits in hippocampal neurons. J. Biol. Chem. **284**(19), 13077–13085 (2009)
3. Härtel, S., Jara, J., Lemus, C.G., Concha, M.L. : 3D morpho-topological analysis of asymmetric neuronal morphogenesis in developing zebrafish. In: Tavares, J., Natal, J.R. (eds.) Computational Modelling of Objects Represented in Images. Fundamentals, Methods and Applications, vol. 6, pp. 215–220. Taylor and Francis, New York (2007)
4. Gustafsson, M.G., Shao, L., Carlton, P.M., Wang, C.J., Golubovskaya, I.N., Cande, W.Z., Agard, D.A., Sedat, J.W.: Three-dimensional resolution doubling in wide-field fluorescence microscopy by structured illumination. Biophys. J. **94**(12), 4957–4970 (2008)
5. Hell, S.W., Nagorni, M.: 4Pi confocal microscopy with alternate interference. Opt. Lett. **23**(20), 1567–1569 (1998)
6. Betzig, E., Patterson, G.H., Sougrat, R., Lindwasser, O.W., Olenych, S., Bonifacino, J.S., Davidson, M.W., Lippincott-Schwartz, J., Hess, H.F.: Imaging intracellular fluorescent proteins at nanometer resolution. Science **313**(5793), 1642–1645 (2006)
7. Hell, S.W., Dyba, M., Jakobs, S.: Concepts for nanoscale resolution in fluorescence microscopy. Curr. Opin. Neurobiol. **14**(5), 599–609 (2004)
8. Keller, P.J., Stelzer, E.H.: Quantitative in vivo imaging of entire embryos with digital scanned laser light sheet fluorescence microscopy. Curr. Opin. Neurobiol. **18**(6), 624–632 (2008)
9. Aubert, G., Kornprobst, P.: Mathematical Problems in Image Processing. Partial Differential Equations and the Calculus of Variations, vol. 147. Applied Mathematical Sciences. Springer, Berlin (2006)
10. Fanani, M.L., De Tullio, L., Hartel, S., Jara, J., Maggio, B.: Sphingomyelinase-induced domain shape relaxation driven by out-of-equilibrium changes of composition. Biophys. J. **96**(1), 67–76 (2009)
11. Fanani, M.L., Härtel, S., Maggio, B., De Tullio, L., Jara, J., Olmos, F., Oliveira, R.G.: The action of sphingomyelinase in lipid monolayers as revealed by microscopic image analysis. Biochim. Biophys. Acta **1798**(7), 1309–1323 (2010)
12. Fidorra, M., Heimburg, T., Seeger, H.M.: Melting of individual lipid components in binary lipid mixtures studied by FTIR spectroscopy, DSC and Monte Carlo simulations. Biochim. Biophys. Acta **1788**(3), 600–607 (2009)
13. Härtel, S., Fanani, M.L., Maggio, B.: Shape transitions and lattice structuring of ceramide-enriched domains generated by sphingomyelinase in lipid monolayers. Biophys. J. **88**(1), 287–304 (2005)
14. Hubený, J., Ulman, V., Matula, P.: Estimating large local motion in live-cell imaging using variational optical flow, towards motion tracking in live cell imaging using optical flow. In: Proceedings of VISAPP 2007, Second International Conference on Computer Vision Theory and Applications, pp. 542–548 (2007)
15. Hamou, A.K., El-Sakka, M.R.: Optical flow active contours with primitive shape priors for echocardiography. EURASIP J. Adv. Signal Process **2010**, 1–11 (2010)
16. Baraldi, P., Sarti, A., Lamberti, C., Prandini, A., Sgallari, F.: Evaluation of differential optical flow techniques on synthesized echo images. IEEE Trans. Biomed. Eng. **43**(3), 259–272 (1996)
17. Abramoff, M.D., Viergever, M.A.: Computation and visualization of three-dimensional soft tissue motion in the orbit. IEEE Trans. Med. Imaging **21**(4), 296–304 (2002)
18. Roberts, T.J., McKenna, S.J., Du, C.J., Wuyts, N., Valentine, T.A., Bengough, A.G.: Estimating the motion of plant root cells from in vivo confocal laser scanning microscopy images. Mach. Vis. Appl. **21**, 921–939 (2010)
19. Ben-Tekaya, H., Miura, K., Pepperkok, R., Hauri, H.P.: Live imaging of bidirectional traffic from the ERGIC. J. Cell Sci. **118**(2), 357–367 (2005)
20. Lombardot, B., Luengo-Oroz, M., Melani, C., Faure, E., Santos, A., Peyrieras, N., Ledesma-Carbayo, M., Bourgine, P.: Evaluation of four 3d non rigid registration methods applied to early zebrafish development sequences. MIAAB MICCAI (2008)
21. Gerencser, A.A., Nicholls, D.G.: Measurement of instantaneous velocity vectors of organelle transport: mitochondrial transport and bioenergetics in hippocampal neurons. Biophys. J. **95**(6), 3079–3099 (2008)
22. Buibas, M., Yu, D., Nizar, K., Silva, G.: Mapping the spatiotemporal dynamics of calcium signaling in cellular neural networks using optical flow. Ann. Biomed. Eng. **38**(8), 2520–2531 (2010)
23. Melani, C., Campana, M., Lombardot, B., Rizzi, B., Veronesi, F., Zanella, C., Bourgine, P., Mikula, K., Peyrieras, N., Sarti, A.: Cells tracking in a live zebrafish embryo. In: Conf Proc IEEE Eng Med Biol Soc 2007, pp. 1631–1634 (2007)
24. Horn, B.K.P., Schunck, B.G.: Determining optical flow. Artif. Intell. **17**, 185–204 (1981)
25. Bruhn, A., Weickert, J., Feddern, C., Kohlberger, T., Schnorr, C.: Variational optical flow computation in real time. IEEE Trans. Image Process. **14**(5), 608–615 (2005)
26. Papenberg, N., Bruhn, A., Brox, T., Didas, S., Weickert, J.: Highly accurate optic flow computation with theoretically justified warping. Int. J. Comput. Vis. **67**(2), 141–158 (2006)
27. Bruhn, A., Weickert, J., Schnörr, C. : Combining the advantages of local and global optic flow methods. In: van Gool, L. (ed.) Proc. 24th DAGM Symposium on Pattern Recognition, vol. 2449, pp. 454–462. Springer, Zurich (2002)
28. Bruhn, A., Weickert, J., Schnörr, C.: Lucas/Kanade meets Horn/Schunck: combining local and global optic flow methods. Int. J. Comput. Vis. **61**(3), 211–231 (2005)
29. Bruhn, A., Weickert, J., Feddern, C., Kohlberger, T., Schnorr, C.: Real-time optic flow computation with variational methods. Proc. Comput. Anal. Images Patterns **2756**, 222–229 (2003)
30. Lucas, B.D., Kanade, T.: An iterative image registration technique with an application to stereo vision. In: International Joint Conference on Artificial Intelligence, vol. 3, pp. 674–679 (1981)
31. Sorensen, T.S., Noe, K.O., Christoffersen, C.P.V., Kristiansen, M., Mouridsen, K., Osterby, O., Brix, L.: Active contours in optical flow fields for image sequence segmentation. In: Biomedical Imaging: From Nano to Macro, 2010 IEEE International Symposium on. pp. 916–919 (2010)
32. Cornelius, N., Kanade, T.: Adapting optical-flow to measure object motion in reflectance and X-ray image sequences. In: Proceedings of the ACM SIGGRAPH/SIGART Interdisciplinary Workshop on Motion, pp. 145–153 (1986)
33. Castro, J., Ruminot, I., Porras, O.H., Flores, C.M., Hermosilla, T., Verdugo, E., Venegas, F., Härtel, S., Michea, L., Barros, L.F.: ATP steal between cation pumps: a mechanism linking Na^+ influx to the onset of necrotic Ca^{2+} overload. Cell Death Different. **13**, 1675–1685 (2006)
34. Härtel, S., Zorn-Kruppa, M., Tykhonova, S., Alajuuma, P., Engelke, M., Diehl, H.: Staurosporine-induced apoptosis in human cornea epithelial cells in vitro. Cytometry **08**, 15–23 (2003)
35. Sanchez, G., Escobar, M., Pedrozo, Z., Macho, P., Domenech, R., Hartel, S., Hidalgo, C., Donoso, P.: Exercise and tachycardia increase NADPH oxidase and ryanodine receptor-2 activity: possible role in cardioprotection. Cardiovasc. Res. **77**(2), 380–386 (2008)
36. Espinosa, A., Garcia, A., Hartel, S., Hidalgo, C., Jaimovich, E.: NADPH oxidase and hydrogen peroxide mediate insulin-induced calcium increase in skeletal muscle cells. J. Biol. Chem. **284**(4), 2568–2575 (2009)

37. Parra, V., Eisner, V., Chiong, M., Criollo, A., Moraga, F., Garcia, A., Hartel, S., Jaimovich, E., Zorzano, A., Hidalgo, C., Lavandero, S.: Changes in mitochondrial dynamics during ceramide-induced cardiomyocyte early apoptosis. Cardiovasc. Res. **77**(2), 387–397 (2008)
38. Box, G.E.P., Muller, M.E.: note on the generation of random normal deviates. Ann. Math. Stat. **29**, 610–611 (1958)
39. Barron, J.L., Fleet, D.J., Beauchemin, S.S.: Performance of optical-flow techniques. Int. J. Comput. Vis. **12**(1), 43–77 (1994)
40. Costes, S.V., Daelemans, D., Cho, E.H., Dobbin, Z., Pavlakis, G., Lockett, S.: Automatic and quantitative measurement of protein-protein colocalization in live cells. Biophys. J. **86**, 3993–4003 (2004)
41. Comeau, J.W., Kolin, D.L., Wiseman, P.W.: Accurate measurements of protein interactions in cells via improved spatial image cross-correlation spectroscopy. Mol. Biosyst. **4**, 672–685 (2008)
42. Ruhnau, P., Kohlberger, T., Schnörr, C., Nobach, H.: Variational optical flow estimation for particle image velocimetry. Exp. Fluids **38**(1), 21–32 (2005)
43. Demandolx, D., Davoust, J.: Multicolour analysis and local image correlation in confocal microscopy. J. Microsc. **185**, 21–36 (1997)
44. Lachmanovich, E., Shvartsman, D.E., Malka, Y., Botvin, C., Henis, Y.I., Weiss, A.M.: Co-localization analysis of complex formation among membrane proteins by computerized fluorescence microscopy: application to immunofluorescence co-patching studies. J. Microsc. **212**, 122–131 (2003)
45. van Kempen, G.: Image Restoration in Fluorescence Microscopy. Technische Universiteit Delft, Netherlands (1999)
46. Bruhn, A., Weickert, J., Kohlberger, T., Schnorr, C.: A multigrid platform for real-time motion computation with discontinuity-preserving variational methods. Int. J. Comput. Vis. **70**(3), 257–277 (2006)
47. Hirokawa, N., Noda, Y.: Intracellular transport and kinesin superfamily proteins, KIFs: structure, function, and dynamics. Physiol. Rev. **88**(3), 1089–1118 (2008)
48. Racine, V., Sachse, M., Salamero, J., Fraisier, V., Trubuil, A., Sibarita, J.B.: Visualization and quantification of vesicle trafficking on a three-dimensional cytoskeleton network in living cells. J. Microsc. **225**(Pt 3), 214–228 (2007)
49. Broeke, J.H., Ge, H., Dijkstra, I.M., Cemgil, A.T., Riedl, J.A., Cornelisse, L.N., Toonen, R.F., Verhage, M., Fitzgerald, W.J.: Automated quantification of cellular traffic in living cells. J. Neurosci. Methods **178**(2), 378–384 (2009)
50. Misko, A., Jiang, S., Wegorzewska, I., Milbrandt, J., Baloh, R.H.: Mitofusin 2 is necessary for transport of axonal mitochondria and interacts with the Miro/Milton complex. J. Neurosci. **30**(12), 4232–4240 (2010)

Author Biographies

José Delpiano received his diploma in Electrical Engineering from Pontificia Universidad Católica de Chile (Santiago, Chl) in 2004 and became a lecturer at Universidad de los Andes (Santiago, Chl). In 2007, he received a Chilean government scholarship for graduate studies. He has served as reviewer in the IEEE International Conference on Neural Networks from 2007. During part of 2010 he was an academic visitor at Department of Computing, Imperial College London, UK. Currently, he is pursuing a PhD in Electrical Engineering at Universidad de Chile (Santiago, Chl). His research interests are biomedical image analysis and computer vision.

Jorge Jara is a Civil Engineer in Informatics at the University Austral of Chile (Valdivia, Chl). In 2007, he received the first prize in the Digital Theses Contest (Universia & País Digital Foundation) for undergraduate students in Chile. Presently, he is a PhD student of the Department of Computer Sciences, University of Chile (Santiago, Chl). He joined the Laboratory of Scientific Image Processing (SCIAN-Lab) as an undergraduate student of computer sciences, working with variational/PDE based active contour models for 2D/3D segmentation and characterization of biological structures in confocal microscopy images. He is interested in reliable segmentation techniques based on mathematical-computational models. Currently, he is working on his PhD research topic, related to segmentation and dynamics characterization of 3D structures and complexes in time-lapse microscopy images.

Jan Scheer studied Medical Informatics at the Ruprecht-Karls-University (Heidelberg, Ger) and spent one year studying Computer Science at the Napier University Edinburgh (Edinburgh, Scotland, UK). He wrote his diploma thesis in the field of biomedical image analysis at the Tissue Imaging & Analysis Center (TIGA) of the University of Heidelberg. He developed a semi-automated tool for the quantification of epithelial protein expression patterns. The tool was designed for the analysis of epithelial images in the Human Protein Atlas. Presently, he is working on the optical flow techniques for motion analysis at the Laboratory of Scientific Image Processing (SCIAN-Lab) at the Medical Faculty of the University of Chile.

Omar A. Ramírez received his PhD in Biomedical Sciences at the University of Chile (Santiago, Chl). He is currently working as a Post-Doc at the Laboratory of Scientific Image Processing (SCIAN-Lab). He was Co-Investigator of the FONDECYT project "Partial Differential Equations for 3D Photon Denoising, Optical Flow and Adjacent Active Surface Models for High Throughput in vivo Spinning Disk Microscopv, and presently pursues the Post-Doc project "Structure and Dynamics of the Endoplasmic Reticulum (ER): Molecular Mechanisms at the Interface of Form and Function". He formed part of the initiative Exzellenzzentrum Santiago de Chile-Heidelberg: Center of Excellence for Innovative Research and Education Medical Informatics as a project coordinator in Medical Informatics Santiago-Heidelberg. His expertise is neuroscience at cellular and subcellular levels, and he is interested in understanding how the morphology of the ER is coupled to synaptic function affecting processes like receptor delivery to synapses. His research focuses on the molecular mechanisms that shape and regulate the ER structure mainly using genetic tools, confocal microscopy and image proccessing. His research contributes to the development of novel forms of parametrization of the ER images to extract relevant quantitative information of its structure.

Javier Ruiz-del-Solar received his diploma in Electrical Engineering and the MS degree in Electronic Engineering from the Technical University Federico Santa Maria (Valparaíso, Chl) in 1991 and 1992, respectively, and the Doctor-Engineer degree from the Technical University of Berlin (Ger) in 1997. In 1998 he joined the Electrical Engineering Department of the Universidad de Chile (Santiago, Chl) as Assistant Professor. In 2001 he became Director of the Robotics Laboratory, in 2005 Associate Professor and in 2011 Full Professor. His research interests include mobile robotics, human-robot interaction, and face analysis. Dr. Ruiz-del-Solar is recipient of the IEEE RAB Achievement Award 2003, RoboCup Engineering Challenge Award 2004, RoboCup @Home Innovation Award 2007, and RoboCup @Home Innovation Award 2008. Since 2006 he has been a Senior Member of the IEEE, and since 2008 a Distinguished Lecturer of the IEEE Robotics and Automation Society. He is currently Director of the Advanced Mining Technology Center at the Universidad de Chile.

Steffen Härtel studied physics at the University Johann Wolfgang von Goethe (Frankfurt, Ger), at the Universidad de Córdoba (Arg), at the Universidad Austral de Chile (Valdivia, Chl), and at the University of Bremen (Ger). He received fellowships from the DAAD and the Bremer Studienfonds. His PhD thesis was honored with summa cum laude and he received the Bremer Studienpreis in combination with the special award of the Bruker Daltonik GmbH. In 2000/2001, he worked as principal investigator at the TZI (Center for Technology and Informatics, Bremen, Ger), financed by the DfG. Between 2001 and 2003, he received a Feodor Lynen Fellowship by the Alexander von Humboldt Foundation (Ger) in combination with a postdoctoral fellowship of CONICET (Arg) and worked in Bruno Maggio laboratory's at the CIQUIBIQ (Córdoba, Arg). In May of 2003, he joined the laboratory of Felipe Barros at the Centro de Estudios Científicos (CECS, Valdivia, Chl) with a 3-year postdoctoral fellowship financed by FONDECYT (Chile). Since 2006, he is leading the Laboratory of Scientific Image Processing (SCIAN-Lab, www.scian.cl) as Assistant Professor at the Faculty of Medicine of the University of Chile (Santiago, Chl). He is Director of the Centro de Espermiogramas Digitales Asistidos por Internet (CED·AI), founder of the Advanced Imaging & Bioinformatics Initiative (AI·BI, www.aibi.cl), and Associate Investigator of the Biomedical Neuroscience Institute (BNI).